Tunable diode laser absorption spectroscopy-based tomography system for on-line monitoring of two-dimensional distributions of temperature and H2O mole fraction

AIP | Review of Scientific Instruments

Tunable diode laser absorption spectroscopy-based tomography system for on-line monitoring of two-dimensional distributions of temperature and H2O mole fraction

Lijun Xu, Chang Liu, Wenyang Jing, Zhang Cao, Xin Xue, and Yuzhen Lin

Citation: Review of Scientific Instruments **87**, 013101 (2016); doi: 10.1063/1.4939052
View online: http://dx.doi.org/10.1063/1.4939052
View Table of Contents: http://scitation.aip.org/content/aip/journal/rsi/87/1?ver=pdfcov
Published by the AIP Publishing

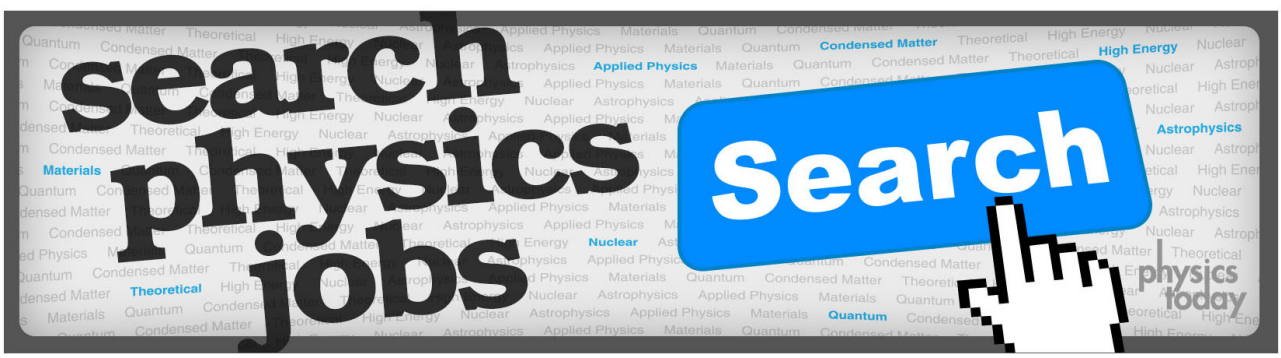

Tunable diode laser absorption spectroscopy-based tomography system for on-line monitoring of two-dimensional distributions of temperature and H_2O mole fraction

Lijun Xu,[1,2,a)] Chang Liu,[1,2] Wenyang Jing,[1,2] Zhang Cao,[1,2] Xin Xue,[3] and Yuzhen Lin[3]
[1]*School of Instrument Science and Opto-Electronic Engineering, Beihang University, Beijing 100191, China*
[2]*Ministry of Education's Key Laboratory of Precision Opto-Mechatronics Technology, Beijing 100191, China*
[3]*School of Energy and Power Engineering, Beihang University, Beijing 100191, China*

(Received 24 August 2015; accepted 13 December 2015; published online 4 January 2016)

To monitor two-dimensional (2D) distributions of temperature and H_2O mole fraction, an on-line tomography system based on tunable diode laser absorption spectroscopy (TDLAS) was developed. To the best of the authors' knowledge, this is the first report on a multi-view TDLAS-based system for simultaneous tomographic visualization of temperature and H_2O mole fraction in real time. The system consists of two distributed feedback (DFB) laser diodes, a tomographic sensor, electronic circuits, and a computer. The central frequencies of the two DFB laser diodes are at 7444.36 cm^{-1} (1343.3 nm) and 7185.6 cm^{-1} (1391.67 nm), respectively. The tomographic sensor is used to generate fan-beam illumination from five views and to produce 60 ray measurements. The electronic circuits not only provide stable temperature and precise current controlling signals for the laser diodes but also can accurately sample the transmitted laser intensities and extract integrated absorbances in real time. Finally, the integrated absorbances are transferred to the computer, in which the 2D distributions of temperature and H_2O mole fraction are reconstructed by using a modified Landweber algorithm. In the experiments, the TDLAS-based tomography system was validated by using asymmetric premixed flames with fixed and time-varying equivalent ratios, respectively. The results demonstrate that the system is able to reconstruct the profiles of the 2D distributions of temperature and H_2O mole fraction of the flame and effectively capture the dynamics of the combustion process, which exhibits good potential for flame monitoring and on-line combustion diagnosis. [http://dx.doi.org/10.1063/1.4939052]

I. INTRODUCTION

Non-invasive measurements of flame temperature and species mole fractions are of great interests in flame monitoring and combustion diagnosis. Empowered by fast development of the room-temperature and narrow-linewidth laser diodes, tunable diode laser absorption spectroscopy (TDLAS) technique has been extensively employed to accurately measure the flame temperature and species mole fractions even in harsh environments.[1–4] Traditional line-of-sight TDLAS technique is capable of measuring path-averaged information along the laser beam with fast response and high sensitivity. However, it suffers from limitations in recovering spatially resolved information for a majority of combustion cases with non-uniform flames.[5] In our previous work, although the nonuniform flame parameters along the laser path were retrieved by using multi-spectral line-of-sight technique, *a priori* information of the temperature distribution tendency must be provided,[6] which, to some extent, restricts the application of this method in practical combustion cases.

In recent years, many efforts have been directed at combining line-of-sight TDLAS with tomographic concept to retrieve the two-dimensional (2D) distributions of temperature and species mole fractions.[7–13] For instance, Wondraczek *et al.* built a laser-tomographic imaging system and acquired the distribution of carbon monoxide in a laminar flame by making multiple laser beams penetrate a rotating burner.[13] Wang *et al.* designed a laboratorial TDLAS-based tomography system and reconstructed 2D distributions of NH_3 mole fraction by simultaneously rotating four laser beams on the rotating platforms.[12] However, rotation of the target or the probing beams undermines the temporal responses of the systems, which are unable to be used for dynamic flames. By sweeping the laser wavelength over a wide spectral range, hyperspectral tomography techniques are capable of reconstructing the 2D distributions of temperature and species mole fractions with high spatial resolution. For example, Ma *et al.* built a hyperspectral tomography system by using Fourier-domain mode-locked laser sources to detect 2D distributions of temperature and H_2O mole fraction at the exhaust plane of a J85 engine.[14] Cai and Kaminski introduced a broad bandwidth and frequency-agile laser source for tomographic imaging of temperature, species mole fractions, and pressure in a reactive flow.[15] To realize hyperspectral tomography, lineshapes of the multiple molecular transitions were fitted and used to retrieve the flame parameters through nonlinear optimizations. Obviously, complex calculations are needed when implementing the hyperspectral tomography, which are far beyond the handling capacity of a system-on-chip and should be carried out off-line using a more powerful computer.

a)Author to whom correspondence should be addressed. Electronic mail: lijunxu@buaa.edu.cn

However, in practical combustion scenarios such as thermal power plants and incinerator facilities, the distributions of temperature and species mole fractions should be measured *in situ* and in real time, in order to provide important feedback to the boiler-control system.[16] Moreover, in swirl-stabilized combustors of gas turbines, the combustion process should be monitored in an on-line manner to investigate the mechanisms driving combustion instabilities.[17] In this way, combustion process can be observed in real time and hence adjusted in time if required, which will contribute to improving combustion stability and efficiency and minimizing pollutant emissions. Therefore, it is necessary to develop an on-line measuring device to monitor combustion status.

In this paper, we developed an on-line TDLAS-based tomography system to monitor the 2D distributions of temperature and H_2O mole fraction within a flame. Based on the stationary TDLAS-based tomographic sensor designed in our previous work,[18] we developed compact and integrated electronic circuits that contain distributed feedback (DFB) laser control unit, photoelectric detecting unit, and central processing unit with a shared-bus interconnection. Tomographic images of the 2D distributions of temperature and H_2O mole fraction are reconstructed in an on-line manner and dynamically displayed by the computer.

II. THEORETICAL BACKGROUND

The physical and mathematical backgrounds of TDLAS-based tomography and the on-line Voigt lineshape fitting have been detailed in Refs. 18 and 19, respectively. Here, we briefly summarize the theories for convenience. When a laser beam at a frequency v [cm^{-1}] enters a flame with a total path length of L [cm], the transmitted laser intensity I_t is related to the incident laser intensity I_0 by

$$\left(\frac{I_t}{I_0}\right)_v = \exp\left(-\int_0^L P(x)X_{abs}(x)S[T(x)]\phi_v \mathrm{d}l\right), \quad (1)$$

where $P(x)$ [atm] is the local total pressure, $S[T(x)]$ [cm^{-2} atm^{-1}] is the temperature dependent line strength of molecular transition, $X_{abs}(x)$ is the local mole fraction of the absorbing species, ϕ_v [cm] is the line-shape function. The absorbance α_v is defined as

$$\alpha_v = -\ln\left(\frac{I_t}{I_0}\right)_v = \int_0^L P(x)X_{abs}(x)S[T(x)]\phi \mathrm{d}l. \quad (2)$$

Because the line-shape function ϕ is normalized, so that $\int_{-\infty}^{\infty}\phi \mathrm{d}v \equiv 1$, integrated absorbance A_v of the molecular transition can be inferred from Eq. (2) as

$$A_v = \int_{-\infty}^{+\infty}\alpha_v \mathrm{d}v = \int_0^L P(x)X_{abs}(x)S[T(x)]\phi \mathrm{d}l. \quad (3)$$

By using a combination of Gauss full width at half maximum (FWHM) w_G and Lorentz FWHM w_L, ϕ in Eq. (2) is generally expressed as

$$\phi_V(v) = \frac{2}{w_G}\sqrt{\frac{\ln 2}{\pi}}\frac{a}{\pi}\int_{-\infty}^{+\infty}\frac{\exp(-y^2)}{a^2+(w-y)^2}\mathrm{d}y, \quad (4)$$

where the variables $a = \sqrt{\ln 2}w_L/w_G$, $w = 2\sqrt{\ln 2}(v-v_0)/w_G$, and $y = 2u\sqrt{\ln 2}/w_G$. Equation (4) is widely known as the Voigt lineshape function. According to Eqs. (3) and (4), the absorbance α_v can be represented by a product of A_v and ϕ_V as follows:

$$\begin{aligned}\alpha_v(v) &= A_v \cdot \phi_V(v) \\ &= A_v \cdot \frac{2}{w_G}\sqrt{\frac{\ln 2}{\pi}}\frac{a}{\pi}\int_{-\infty}^{+\infty}\frac{\exp(-y^2)}{a^2+(w-y)^2}\mathrm{d}y. \end{aligned} \quad (5)$$

With the raw absorbance in hand, Gauss-Newton nonlinear fitting method is implemented to obtain the parameters including both w_G and w_L by a system-on-chip, which can be used to calculate the integrated absorbance A_v.[19]

The mathematical formulation of the TDLAS-based tomography problem is schematically illustrated in Fig. 1. The circular region of interest (ROI) is discretized into N (=332 in this case) cells. Given that the radius of the ROI is 3 cm, a spacing of 0.3 cm between the neighboring cells along both the directions of x- and y-axes is obtained. In the jth cell, the flame parameters, i.e., P_j, T_j, and X_j are assumed to be constant. The density of the integrated absorbance in the jth cell $a_{v,j}$ is defined as a product of P_j, $S(T_j)$, and X_j, i.e., $a_{v,j} = [PS(T)X]_{v,j}$. For the ith laser beam, the sampled integrated absorbance $A_{v,i}$ is expressed as

$$A_{v,i} = \sum_{j=1}^{N} a_{v,j}L_{ij}, \quad (6)$$

where L_{ij} is the path length of the ith laser beam penetrating the jth cell. For a total of M laser beams, Eq. (6) can be compactly written as

$$\boldsymbol{L}\boldsymbol{a}_v = \boldsymbol{A}_v, \quad (7)$$

where the $M \times N$ matrix $\boldsymbol{L}$ is

$$\boldsymbol{L} = \begin{bmatrix} L_{11} & L_{12} & \cdots & L_{1N} \\ L_{21} & L_{22} & \cdots & L_{2N} \\ \vdots & \vdots & \ddots & \vdots \\ L_{M1} & L_{M2} & \cdots & L_{MN} \end{bmatrix}, \quad (8)$$

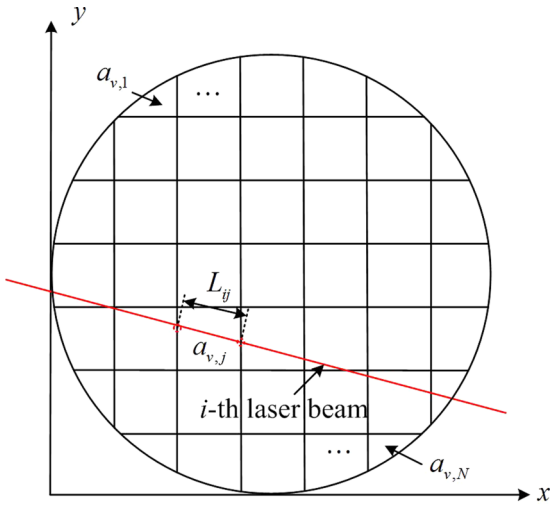

FIG. 1. Geometric description of line-of-sight TDLAS measurement.

the column vector $\boldsymbol{a}_v = (a_{v,1}, a_{v,2}, \ldots, a_{v,N})^T$ and $\boldsymbol{A}_v = (A_{v,1}, A_{v,2}, \ldots, A_{v,M})^T$. $\boldsymbol{a}_v$ at two independent molecular transitions v_1 and v_2, noted as $\boldsymbol{a}_{v_1}$ and $\boldsymbol{a}_{v_2}$, can be calculated by using a modified Landweber algorithm,[20,21] in which the gradient of the least-squares objective function $\|\boldsymbol{L}\boldsymbol{a}_v - \boldsymbol{A}_v\|^2$ is taken with respect to $\boldsymbol{a}_v$,

$$\boldsymbol{a}_v^{k+1} = \boldsymbol{a}_v^k + \lambda_k \boldsymbol{L}^T(\boldsymbol{A}_v - \boldsymbol{L}\boldsymbol{a}_v^k), \tag{9}$$

where $\boldsymbol{a}_v^k$ is the current iteration vector, $\boldsymbol{a}_v^{k+1}$ the new iteration vector, and λ_k the relaxation parameter. It should be noted that λ_k plays an important role in obtaining an accurate and stable solution. The iteration of Eq. (9) converges to a solution $\boldsymbol{a}_v^*$ of $\min\|\boldsymbol{L}\boldsymbol{a}_v - \boldsymbol{A}_v\|^2$ if and only if

$$0 < \lambda_k < 2\left(\left\|\boldsymbol{L}^T\boldsymbol{L}\right\|^2\right)^{-1}. \tag{10}$$

For higher efficiency of the algorithm, a "line search" strategy is employed to compute λ_k in each iteration, instead of using training to determine a fixed relaxation parameter.[22] We can rewrite Eq. (9) as

$$\boldsymbol{a}_v^{k+1} = \boldsymbol{a}_v^k + \lambda_k \boldsymbol{p}^k, \tag{11}$$

where $\boldsymbol{p}^k = \boldsymbol{L}^T(\boldsymbol{A}_v - \boldsymbol{L}\boldsymbol{a}_v^k)$. The "line search" strategy minimizes the error $\left\|\boldsymbol{a}_v^* - \boldsymbol{a}_v^k\right\|^2$ for the next iteration, which leads to the choice

$$\lambda_k = \frac{\boldsymbol{p}^k \cdot (\boldsymbol{a}_v^* - \boldsymbol{a}_v^k)}{\left\|\boldsymbol{p}^k\right\|_2^2}. \tag{12}$$

If we use $\boldsymbol{L}\boldsymbol{a}_v^* = \boldsymbol{A}_v$ and define $\boldsymbol{r}^k = \boldsymbol{A}_v - \boldsymbol{L}\boldsymbol{a}_v^k$, then Eq. (11) can be written as

$$\lambda_k = \frac{\boldsymbol{r}^k \cdot \boldsymbol{r}^k}{\left\|\boldsymbol{L}^T\boldsymbol{r}^k\right\|_2^2}, \quad \boldsymbol{r}^k = \boldsymbol{A}_v - \boldsymbol{L}\boldsymbol{a}_v^k. \tag{13}$$

The convergence is monitored by the relative change of $\boldsymbol{a}_v^{k+1}$ from $\boldsymbol{a}_v^k$, noted as Δ, i.e.,

$$\Delta = \frac{\sum_{j=1}^{N}\left|a_{v,j}^{k+1} - a_{v,j}^k\right|}{\sum_{j=1}^{N}(a_{v,j}^{k+1})}. \tag{14}$$

The iteration stops when Δ is smaller than 0.1%. Finally, the temperature T_j in jth cell can be retrieved from the ratio of $a_{v1,j}$ and $a_{v2,j}$, which is a monotone function of T_j known as the two-color strategy,

$$R = \frac{a_{v1,j}}{a_{v2,j}} = \frac{S_1(T_j)}{S_2(T_j)}. \tag{15}$$

With T_j in hand, the mole fraction X_j can be obtained from Eq. (16) at an atmosphere pressure

$$X_j = \frac{a_{v1,j}}{S_1(T_j)}. \tag{16}$$

III. SYSTEM IMPLEMENTATION

As shown in Fig. 2, the on-line TDLAS-based tomography system mainly includes two DFB laser diodes, a tomographic sensor, electronic circuits, and a personal computer (PC). To be specific, the central frequencies of the two DFB are at 7444.36 cm^{-1} and 7185.6 cm^{-1}, respectively. The tomographic sensor is used to generate fan-beam illumination from five views and produce a total of 60 ray measurements on the photodiode arrays for each molecular transition, as detailed in Ref. 18. The electronic circuits are integrated into a portable case, which not only provide stable temperature and precise current controlling signals for the DFB but also can accurately sample the multi-channel transmitted laser intensities and extract integrated absorbances in real time. The integrated absorbances are transferred to the personal computer, in which the 2D distributions of temperature and

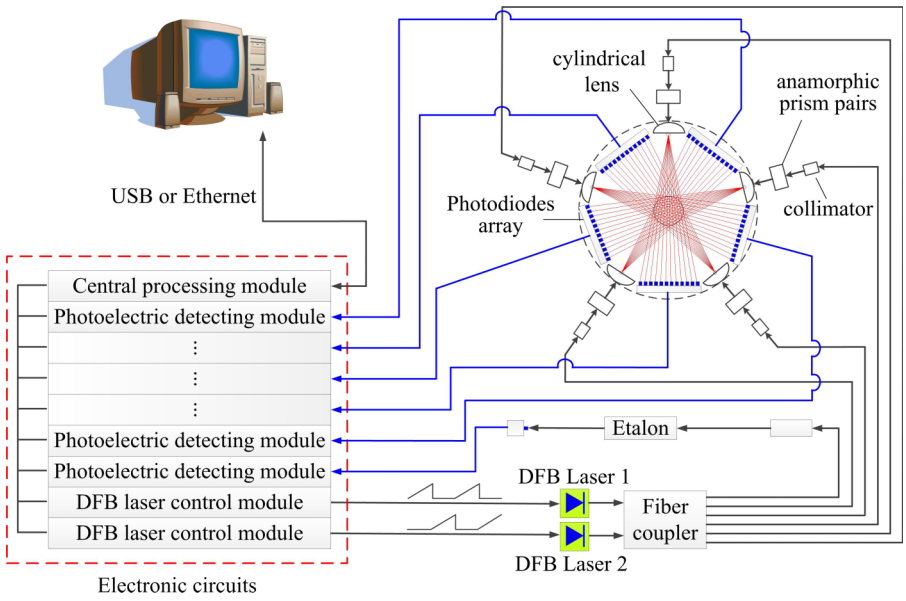

FIG. 2. Schematic of the on-line TDLAS-based tomography system.

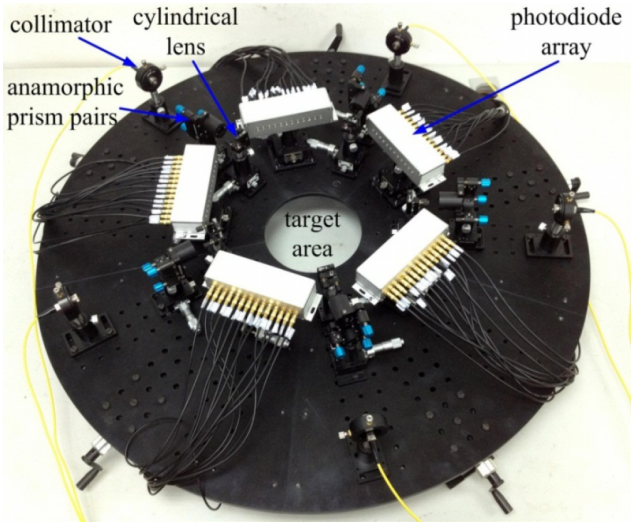

FIG. 3. Layout of the fan-beam TDLAS-based tomographic sensor.

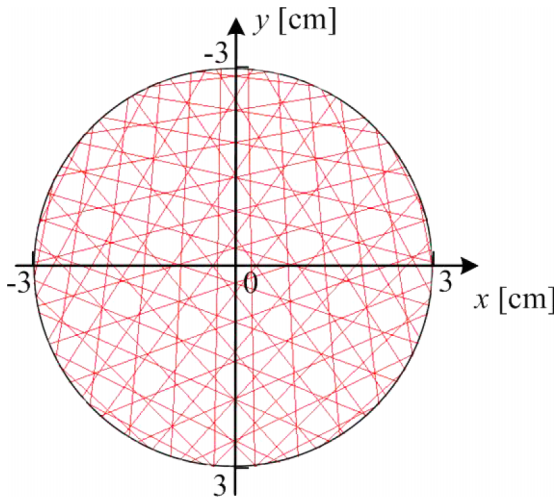

FIG. 4. Arrangements of the fan-beam laser paths in the ROI.

H_2O mole fraction are reconstructed in an on-line manner by using the modified Landweber algorithm.

A. Fan-beam TDLAS-based tomographic sensor

The fan-beam TDLAS-based tomographic sensor is shown in Fig. 3. Two DFB at H_2O molecular transitions of v_1 = 7444.36 cm^{-1} (1343.33 nm) and v_2 = 7185.6 cm^{-1} (1391.67 nm) work in a time division multiplexing scheme,[19,23,24] which is realized by using DFB controllers and the control strategy detailed in Subsections III B 1–III B 3, respectively. The criteria and reason of selecting the transitions of 7444.36 cm^{-1} and v_2 = 7185.6 cm^{-1} were detailed in our previous work.[24] The output laser beam from one of the channels penetrates a Fabry-Pérot interferometer to monitor the frequency during the wavelength scanning, while those from the remaining channels are used to generate fan-beam illumination from five views. To generate the fan-beam illumination, laser in an optic-fiber is first collimated. Then, anamorphic prism pairs and a cylindrical lens are combined to transform the collimated laser to the fan-beam illumination. Five fan-beam generators are placed around a circle with equal angular spaces. The radius of the circle is 14 cm. The span angle of each fan-beam illumination is about 24°, which can cover the ROI with a radius of 3 cm. The arrangements of the fan-beam laser paths in the ROI are shown in Fig. 4. Each fan-beam illumination penetrates the ROI and is detected by 12 equal-spaced photodiodes with a sensitive wavelength range from 900 nm to 1700 nm, with which the transmitted laser intensities can be obtained. For each molecular transition, 60 projections, i.e., $\boldsymbol{A}_v$ in Eq. (7), are extracted from the transmitted laser intensities and used to retrieve $\boldsymbol{a}_v$. It is worth mentioning that if the numbers of fan-beam generators and projections are too small, the two-dimensional distribution cannot be reconstructed accurately. Huge number of fan-beam generators and projections will cause a kind of resource wastage. As detailed in our previous work,[18] the numbers of fan-beam generators and projections were chosen in consideration of the balance between the tomographic accuracy and the complexity of optics of the tomographic sensor.

B. Electronic circuits

As shown in Fig. 5, the electronic circuits contain three units, i.e., DFB laser control unit, photoelectric detecting unit, and central processing unit. The DFB laser control unit contains two modules to provide time division multiplexing control signals to the two DFB. The photoelectric detecting unit contains eight modules. Each module contains eight independent measurement channels. Therefore, a total of eight modules are expanded to acquire 60 projections from 60 measurement channels. The central processing unit contains one module to realize data processing and transfer. All the modules are integrated into a portable case with a shared-bus interconnection. In this way, more individual modules can be flexibly expanded if necessary.

1. DFB laser control module

The output wavelength of the DFB can be coarsely and precisely tuned by the temperature and driving current, respectively. In addition, the output power of the DFB used in this work is dependent on the driving current with a sensitivity of 0.1 mW/mA in its linear region. To provide stable temperature and precise current controlling signals for

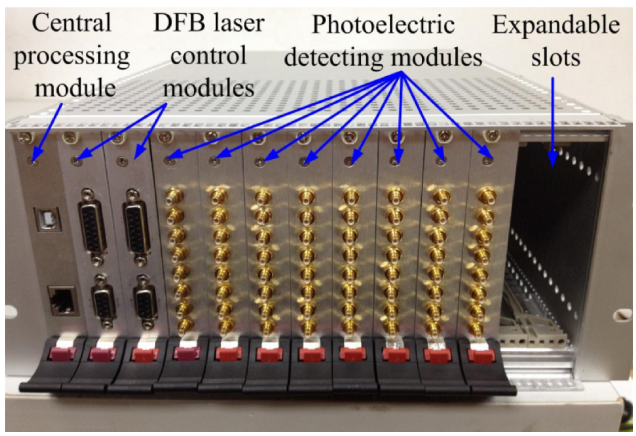

FIG. 5. Portable case that integrates the electronic circuits.

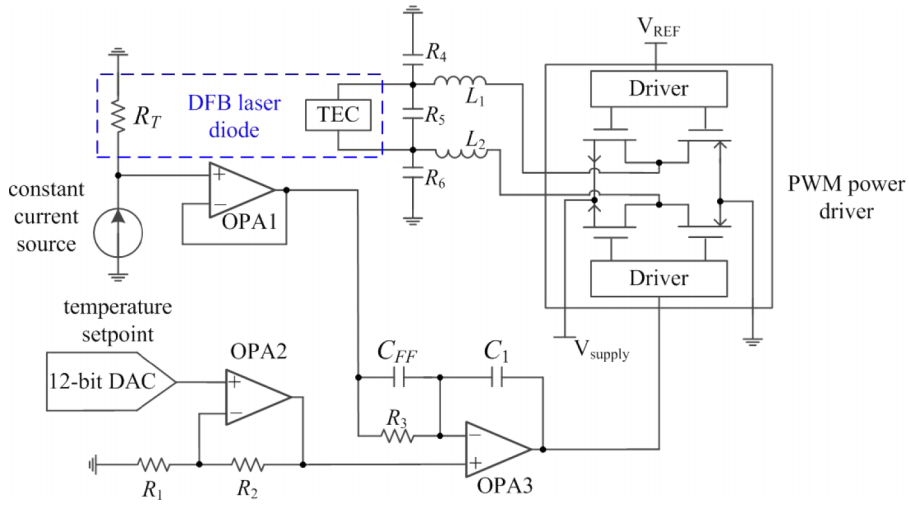

FIG. 6. Schematic of the TEC control loop.

the DFB, the DFB laser control module contains two control loops, i.e., thermo-electric cooler (TEC) and current control loops.[25]

In the TEC control loop, a thermistor driven by a constant current is used to monitor the temperature of the DFB. As shown in Fig. 6, the voltage across the thermistor R_T is applied to the integrator built around an operational amplifier (OPA). As the difference between the thermistor voltage and the setpoint increases, the integrator will ramp up or down, which drives the current through the TEC in either direction, to either heat or cool the TEC by using a Pulse-Width Modulated (PWM) power driver. The DFB used in this work can achieve a temperature dependence sensitivity of about ±0.02 nm/°C. To guarantee the wavelength stability, the uncertainty of the temperature should be maintained within ±0.1 °C, which will result in a change of ±0.002 nm from the center wavelengths of 1391.67 nm and 1343.33 nm, respectively. The temperature setpoint is determined by a 12-bit digital-to-analog converter (DAC) controlled by a Field Programmable Gate Array (FPGA), which can afford a temperature resolution of about 0.03 °C per Least Significant Bit. As the temperature setpoint is changed, the loop will attempt to force the temperature to converge to the setpoint. If the difference between the actual temperature and the setpoint exists, the TEC control loop will operate until the difference disappears. Adding a feedforward capacitor (C_{FF}) to the integrator contributes to greatly reduce the overshoot and the time needed for the loop to stabilize to the new setpoint due to a step change. The resulting operation of the TEC control loop is shown in Fig. 7. The temperature stability for the range from 15 °C to 45 °C is approximately ±0.01 °C at steady state, while the response time for a step change of 4 °C of the setpoint is about 5 s.

The current control loop is shown in Fig. 8. The current setpoint comes from a 14-bit DAC controlled by the FPGA. The current through the laser is sensed with a resistor R_S with high precision and very low temperature drift. The voltage across R_S is amplified using a gain-of-10 instrumentation amplifier (INA). The voltage signal is fed back to an integrator built around OPA1, which integrates difference between the current setpoint and the actual current. The output signal of OPA1 finally drives a linear power amplifier (LPA) to adjust the current. The current control loop is validated using a sinusoidal signal at 50 kHz. As shown in Fig. 9, the voltages across R_S can precisely track the input, denoting that the current control loop can well control the current through the laser.

2. Photoelectric detecting module

In this work, each photoelectric detecting module contains eight independent measurement channels. For each channel, the transmitted laser intensities are transferred by the photodiodes to current signals. To obtain the most precise linear operations, the photodiodes operate with zero bias voltage, i.e., in a photovoltaic mode, as shown in Fig. 10. The photoelectric detecting module is first used to convert the current signals that are produced by the photodiodes to voltage signals by using trans-impedance amplifiers.[26,27] In this work, the current signals produced by the photodiodes are very small, always in the range 10–100 μA. Therefore, a high-feedback resistance R_f and a Field Effect Transistor-input amplifier with ultralow bias current is necessary in the trans-impedance amplifier. Furthermore, a supplemental capacitor C_s is in parallel with

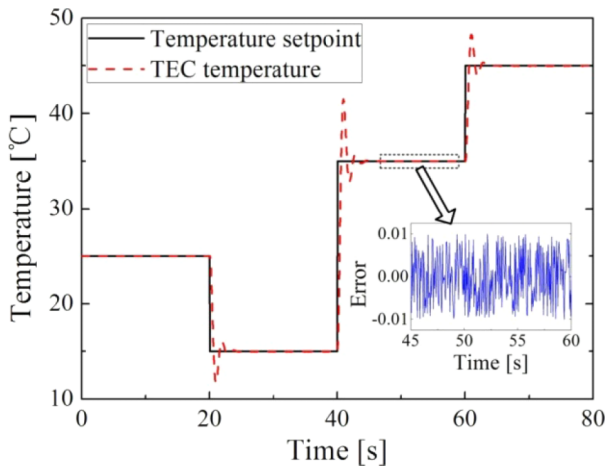

FIG. 7. Response of the TEC control loop for temperature step changes.

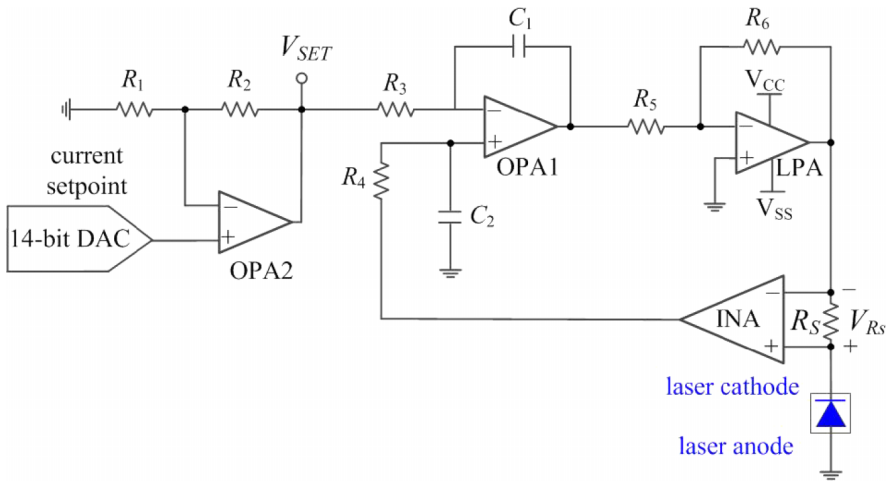

FIG. 8. Schematic of the current control loop.

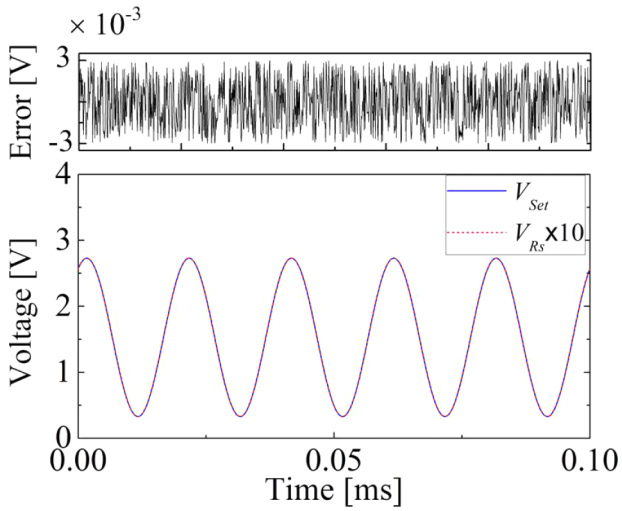

FIG. 9. Response of the current control loop for a sinusoidal input signal.

R_f, which is used to adjust the signal bandwidth and suppress high frequency noises. In conjunction with the 8 × 1 analog switches, voltage signal in each channel can be selected independently and further amplified using an OPA and a programmable-gain amplifier (PGA). The output of the PGA is sampled by a 12-bit analog to digital converter (ADC) with 10 mega samples per second (MSPS). In the circuit, a complex programmable logic device (CPLD) is employed to control the analog switches, PGA, and ADC and transfer the sampled data to the central processing module through a data bus. To examine the signal to noise ratio (SNR) of the circuit, sinusoidal current of the DFB with different magnitudes and frequencies is generated. In this way, we can output laser with different intensities and frequencies. The output laser is detected by a photoelectric detecting channel. The SNR is defined as

$$\mathrm{SNR} = 10\lg \frac{\sum_{i=1}^{N_S} I_{meas,i}^2}{\sum_{i=1}^{N_S} \left(I_{meas,i} - I_{fit,i}\right)^2}, \tag{17}$$

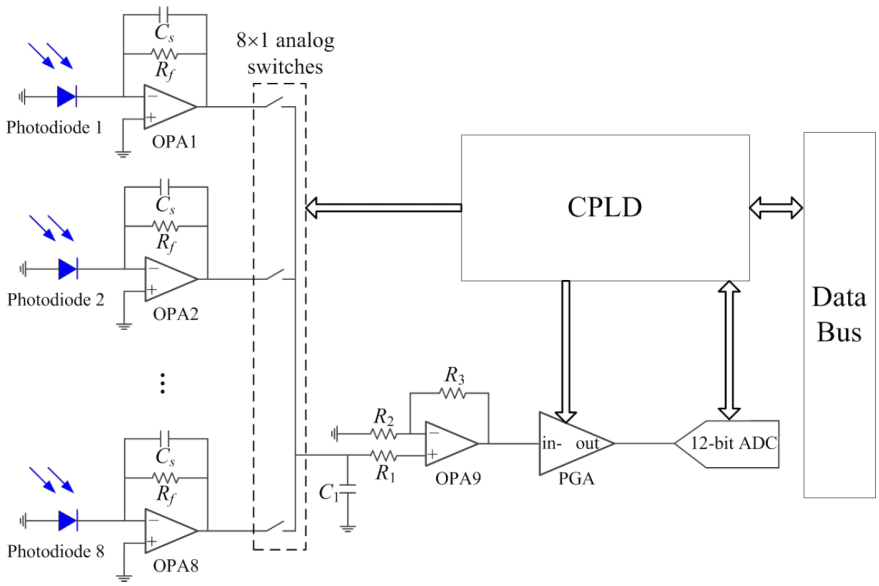

FIG. 10. Schematic of the photoelectric detecting module.

TABLE I. SNRs of a photoelectric detecting channel for output laser with different intensities and frequencies.

f (kHz)	0.5	5	50
I_M (μW)		SNR (dB)	
15.75	43.6	44.2	43.7
103.96	52.7	52.5	53.6
574.36	59.8	59.3	60.2

where N_S is the number of sampled data, I_{meas} is the measured laser intensity, and I_{fit} is the fitted noise-free data from a sine wave. The averaged magnitude of I_{meas}, noted as I_M, is measured by an optical power meter. As illustrated in Table I, larger laser intensity contributes to higher SNR. For the same laser intensity, the SNRs obtained at 0.5 kHz, 5 kHz, and 50 kHz are similar to each other.

3. Central processing module

The functional diagram of the central processing module is shown in Fig. 11. The central processing module mainly contains a FPGA, a DSP, Universal Serial Bus (USB), and Ethernet microcontrollers for data communication. The central processing module has three main functions. First, it provides time division multiplexing control signals to the DFB laser controllers through a data bus. In detail, during a scanning period, the FPGA enables one of the DFB laser controllers. In this way, one DFB is driven by a ramp current, while the other DFB is not. Second, the central processing circuit selects the measurement channel and fits the Voigt lineshape in an on-line manner. To be specific, the FPGA sequentially acquires and pre-processes the received laser intensity from the selected channel of the photoelectric detecting circuit through the data bus. As detailed in our previous work,[19] a total of 50 points, i.e., 10 points on the non-absorption wings and 40 points on the absorption region, are selected by the FPGA. With the selected points, the Voigt lineshape can be fitted by the DSP and thus the integrated absorbance, i.e., the projection, can be calculated. Third, the FPGA sequentially transfers the projections from 60 channels to the computer through the USB or Ethernet port. With all the projections, the modified Landweber algorithm is implemented by the computer to reconstruct the 2D distributions of temperature and H_2O mole fraction.

IV. EXPERIMENTS AND RESULTS

A. Experimental setup

The flame was generated by using a McKenna flat-flame burner. The radius of the burner plug is 3 cm. As shown in Fig. 12, the asymmetric flame profile was generated by putting two steel cubes on D_1 and D_2 regions of the burner plug. The length, width, and height of the cube in the region D_1 are 1 cm, 2 cm, and 1 cm, while those of the cube in region D_2 are 1 cm, 2 cm, and 2 cm, respectively. In this way, the fuel was released only from the place where the burner plug was not blocked, which contributed to the asymmetric flame with non-uniform distributions of temperature and H_2O mole fraction. The measurement was implemented 3 s after the premixed fuel was ignited. The stainless steel cubes were not adequately heated in the measurement period. The origin of the xOy coordinate system in Fig. 12 was at the center of the ROI that was discretized into 332 cells, and thus, a spacing of 0.3 cm between the neighboring cells along both the directions of x- and y-axes is obtained. The height above the burner plug is noted as z. The height of the fan-beam illumination was adjusted to 3 cm above the burner plug. That is to say, the 2D distributions of temperature and H_2O mole fraction on the cross section of the flame at z = 3 cm were reconstructed in real time. As noted in Ref. 18, the ROI with a radius of 3 cm is sufficient to cover the cross section of the flame at z = 3 cm.

In the experiment, the direct absorption spectroscopy modality was adopted. The wavelength tuning speed of each of the two DFB laser diodes was 10 kHz, in other words, the scanning period for each DFB laser diode was 0.1 ms. Therefore, the scanning period was 0.2 ms for the two DFB laser diodes with the time division multiplexing scheme. Given that the DSP (TMS320C6713B, Texas Instruments) was fast enough to fit the Voigt lineshapes in real time, the computer acquired two integrated absorbances at v_1

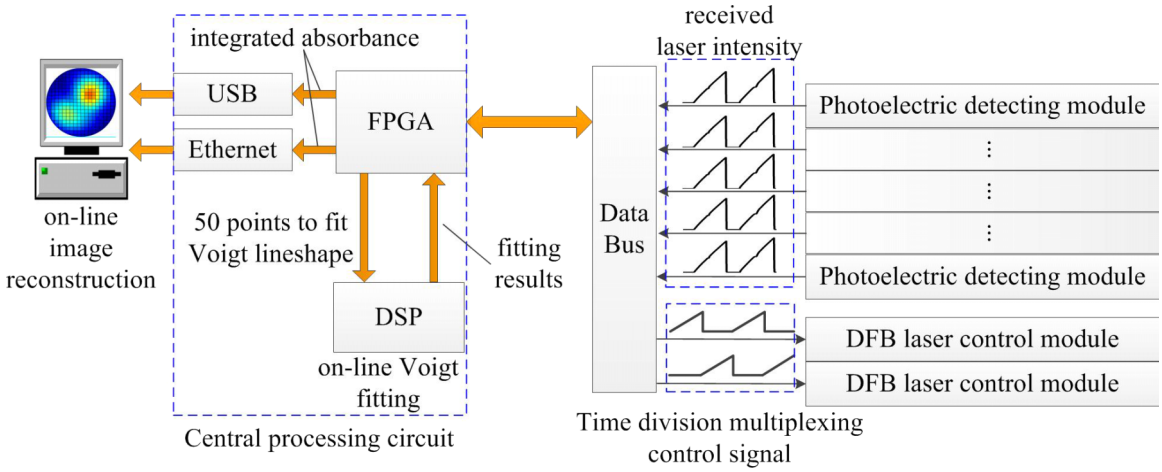

FIG. 11. Functional diagram of the central processing module.

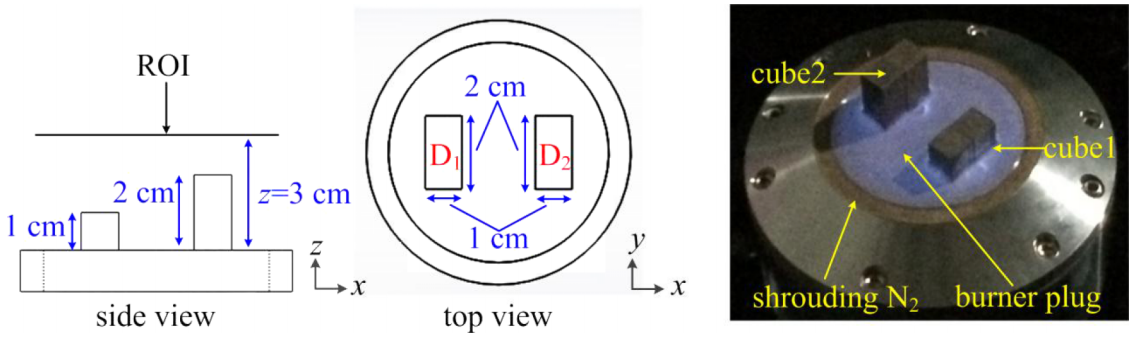

FIG. 12. Experimental setup of the phantom to generate an asymmetric flame with non-uniform distributions of temperature and H_2O mole fraction.

$= 7444.36\ \text{cm}^{-1}$ and $v_2 = 7185.6\ \text{cm}^{-1}$ when a periodic scanning was finished. As illustrated in Subsection III B 3, the transmitted laser intensities of 60 channels were sequentially sampled and preprocessed. The two integrated absorbances for each channel were calculated by the DSP and transferred from the FPGA on the central processing circuit to the computer. Therefore, it took 12 ms (0.2 ms × 60) for the computer to obtain all the projection data from five views to simultaneously reconstruct the images of temperature and H_2O mole fraction. In general, it took about 4 ms for the computer to compute the modified Landweber algorithm. In other words, the computing time is significantly shorter than the time of obtaining all the projection data. Therefore, no processing delay will be brought by the PC to reconstruct the tomographic image by using the Landweber algorithm. The reconstructed 2D distributions of temperature and H_2O mole fraction can be updated and displayed by the computer every 12 ms. It should be noted that the imaging speed of the system, i.e., temporal resolution, should be adjusted according to the dynamic performance of the target flame, which will be further discussed in Subsection IV B.

B. Results and discussions

The on-line TDLAS-based tomography system was first validated by a stable premixed flame with a fixed equivalent ratio of the premixed fuel. In this case, the equivalent ratio of 0.749 was obtained by setting the flow rates of methane and air to 1.2 and 15.25 l/min, respectively. Furthermore, to reduce the impact of convection between the core flame and the surrounding air, shrouding nitrogen with a flow rate of 22.5 l/min was released around the burner plug. It should be noted that all the optics and laser paths except those in the region of interest are purified by nitrogen. In this way, an ambient humidity of 0.065% is obtained using an absorption hygrometer. Given the arrangements of the fan-beam laser paths, the integrated absorbance area of the ith laser beam for the laser path outside the region of interest, i.e., $A_{air,i}$, can be calculated by

$$A_{air,i} = PS(T_{air})X_{air}L_{air,i}, \tag{18}$$

where the pressure P equals 1 atm, T_{air} equals 300 K, and X_{air} equals 0.065%. $L_{air,i}$ is the path length out of the region of interest for the ith laser beam. Therefore, the projection for the ith laser beam, i.e., A_i, can be calculated by subtracting the measured integrated absorbance $A_{meas,i}$ to $A_{air,i}$. In addition, A_1 and $A_{air,1}$ of the transition at 7185.6 cm^{-1} for the 1st laser beam equal 1.14×10^{-2} and 2.92×10^{-4}, respectively. If T_{air} equals to 800 K, $A_{air,1}$ equals to 5.65×10^{-4}. That is to say, even the flame emission causes a large temperature change, the change of $A_{air,1}$ is sufficiently small compared with A_1. Therefore, the impact of flame emission can be neglected.

After obtaining all the projection data from five views, the computer reconstructed one frame image of the temperature, i.e., T^{rec}, and one frame image of H_2O mole fraction, i.e., X^{rec}, as shown in Figs. 13(a) and 13(b), respectively. In consideration of continuous distributions of the temperature and H_2O mole fraction in the flame, a Gaussian low-pass filter of size 3×3 with a standard deviation (σ) of 0.5 is applied

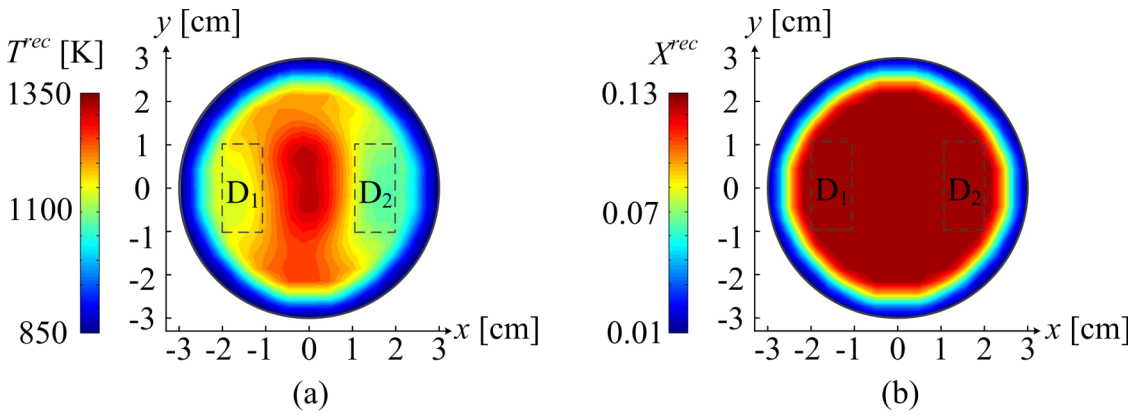

FIG. 13. Reconstructed 2D distributions of (a) temperature and (b) H_2O mole fraction for the phantom in Fig. 12 with a fixed equivalent ratio of 0.749.

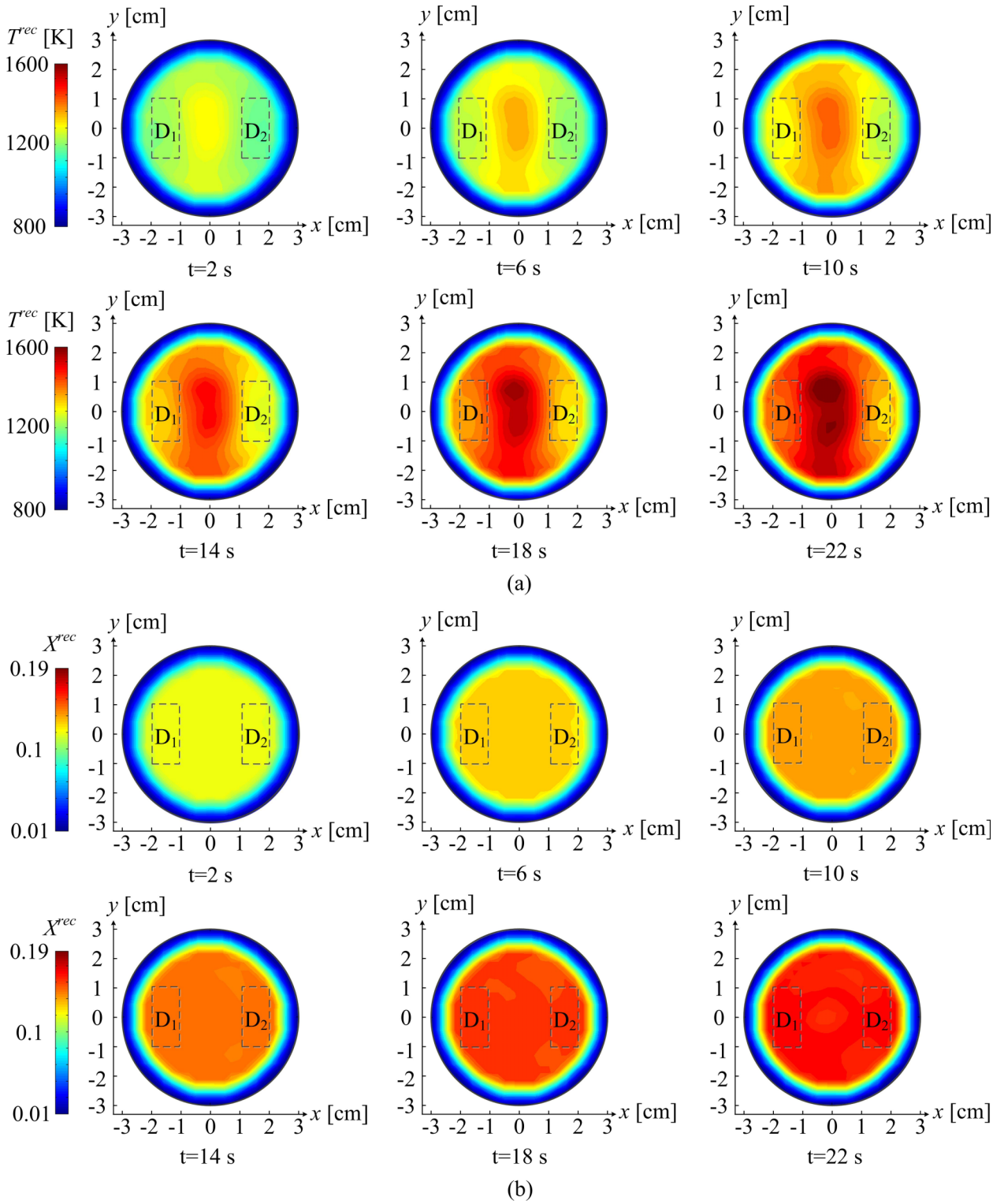

FIG. 14. Reconstructed 2D distributions of (a) temperature and (b) H_2O mole fractions for the phantom in Fig. 12 when the equivalent ratio increases from 0.69 to 1. To realize the time varying equivalent ratio, the flow rate of air was set to 15.25 l/min, while the flow rate of methane was first set to 1.1 l/min and was increased with an interval of 0.1 l/min for every 4 s. When the flame is stabilized, we obtained the T^{rec} and X^{rec} at 2 s, 6 s, 10 s, 14 s, 18 s, and 22 s, respectively.

within each iteration in the modified Landweber algorithm to remove the artifacts and render the inherently ill-posed problem more tractable. As shown in Fig. 13(a), T^{rec} in region D_1 and region D_2 are lower than those in the central region without the cubes. As the top of the cube in region D_2 is closer to the ROI compared with that in region D_1, more heat of the flow transfers to the cube in region D_2. Furthermore, because the height of the cube in region D_1 is lower than that in region D_2, the gaseous mixture flows over the cubes and diffuses to a larger extent in the region D_1 than that in region D_2 at the height of $z = 3$ cm. In this way, much of the combustion heat diffuses over region D_1 than that in region D_2. Therefore, T^{rec} in region D_1 is higher than that in region D_2. As shown in Fig. 13(b), since the flow was premixed, as long

as combustion was complete (and it was in this case), the mole fraction of H_2O would be constant in the core flame.[18] X^{rec} gradually decreases from the center to the boundary due to gas mixing between the combustion products and the shrouding nitrogen at the boundary of the flame. It can be seen that both the reconstructed profiles of T^{rec} and X^{rec} agree well with the expected profiles, denoting that the system is effective to reconstruct the 2D distributions of temperature and H_2O mole fraction.

Furthermore, 100 repetitive measurements were performed to evaluate the variation in the tomographic images in measurement duration of 6 s. The averaged tomographic images of T^{rec} and X^{rec} from 100 measurements, noted as T^{M_rec} and X^{M_rec}, are obtained by averaging the values of temperature and H_2O mole fraction from 100 measurements in each cell. The average normalized difference between T^{rec} and T^{M_rec}, noted as e_T, is defined as

$$e_T = \frac{1}{N}\sum_{j=1}^{N}\left(\left|T_j^{rec} - T_j^{M\_rec}\right| \Big/ T_j^{M\_rec}\right), \tag{19}$$

and the average normalized difference between X^{rec} and X^{M_rec}, noted as e_X, is defined as

$$e_X = \frac{1}{N}\sum_{j=1}^{N}\left(\left|X_j^{rec} - X_j^{M\_rec}\right| \Big/ X_j^{M\_rec}\right). \tag{20}$$

The variability in the tomographic images in the measurement duration of 6 s is therefore quantitatively described by the standard deviations of e_T and e_X obtained from 100 measurements, noted as, σ_T and σ_X, respectively. In this case, σ_T and σ_X equal 1.46×10^{-3} and 1.03×10^{-4}, respectively.

Then, the dynamic performance of the on-line TDLAS-based tomography system was validated by flames with time-varying equivalent ratio. The flow rate of air was set to 15.25 l/min. In the experiment, the flow rate of methane was first set to 1.1 l/min and was increased with an interval of 0.1 l/min for every 4 s. Therefore, for the measurement duration of 24 s, the flow rate of methane was increased from 1.1 l/min to 1.6 l/min, which resulted in an increase in equivalent ratio from 0.69 to 1. The flame was relatively stable even in case of the time varying equivalent ratio. When the flow rate of methane was stabilized, we obtained the T^{rec} and X^{rec} at 2 s, 6 s, 10 s, 14 s, 18 s, and 22 s in the steady state, as shown in Figs. 14(a) and 14(b), respectively. The magnitudes of T^{rec} and X^{rec} are larger in case of a higher equivalent ratio. As shown in Fig. 14(a), for each equivalent ratio, T^{rec} in region D_1 are larger than those in region D_2, while those in the central region without the blocks are larger than those in region D_1 and region D_2. As shown in Fig. 14(b), the uniformity of X^{rec} is significantly better than that of T^{rec} because of the complete combustion of the premixed fuel. Furthermore, compared with the above case of fixed flow rates of methane and air, larger extent of flow disturbance of the gaseous mixture will be caused by the time varying flow rate of methane. In this way, the shrouding nitrogen will mix into the premixed flame, which, to some extent, decreases the uniformity of X^{rec} in the core flame.[18] The results obtained from time varying equivalent ratio show that the on-line TDLAS-based tomography system is capable of capturing the dynamic combustion process of the flame with time varying equivalent ratio.

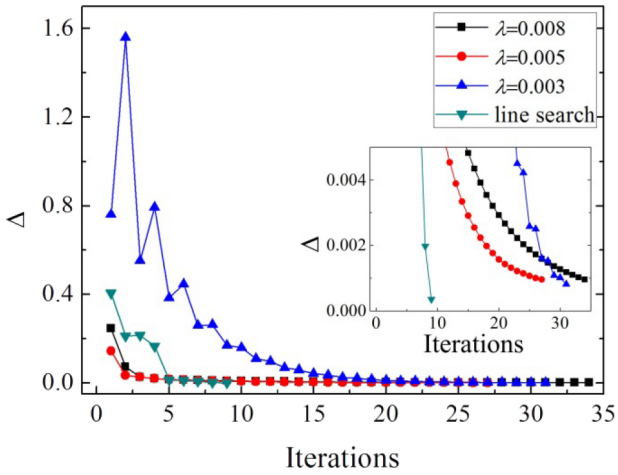

FIG. 15. Dependence of Δ on the iterations when the relaxation parameters are determined by using the "line search" strategy and fixed values of 0.003, 0.005, and 0.008, respectively.

To capture more rapidly changing combustion flames such as turbulent flames in inner engines, the temporal resolution of the system may need to be increased to improve the dynamic performance of the system. There are two main approaches to increase the temporal resolution of the system. One is selecting higher speed DFB or increasing the wavelength scanning speed of the DFB within its upper limit. The other is operating the photoelectric detecting channels in parallel rather than in serial.

As illustrated in Section II, the "line search" strategy is employed to compute the relaxation parameter in each iteration, instead of using the training strategy to determine a fixed relaxation parameter. It should be noted that the "line search" strategy is effective to make the solution to converge fast and improve the efficiency of the algorithm. For 60 projections at the transitions 7185.6 cm^{-1}, i.e., $\boldsymbol{A}_{v1}$, to reconstruct one frame of the image, the iterations were implemented with the relaxation parameters determined by using the "line search" strategy and fixed values, respectively. In each case, Δ in Eq. (14) was calculated after each iteration. As shown in Figure 15, Δ is smaller than 0.1% after the 10th iteration by using the "line search" strategy, denoting that the solution has converged. However, the solutions converged after the 31st, 27th, and 34th iterations for $\Delta = 0.003$, $\Delta = 0.005$, and $\Delta = 0.008$, respectively. Therefore, compared with the cases using fixed relaxation parameters, the "line search" strategy significantly speeds up the convergence.

V. CONCLUSIONS

To realize real-time measurements of 2D distributions of temperature and H_2O mole fraction, an on-line TDLAS-based tomography system was developed in this paper. With the stationary TDLAS-based tomographic sensor and the integrated electronic circuits with a shared-bus interconnection, the integrated absorbances, i.e., the projections along relative laser beams, were fast and accurately obtained by a system-on-

chip. With the projections in hand, the computer is employed to reconstruct the 2D distributions of temperature and H_2O mole fraction in real time. The temporal resolution of the system is 12 ms.

To validate the system, experiments were carried out for the asymmetric premixed flames with a fixed equivalent ratio of 0.749 and a time-varying equivalent ratio from 0.69 to 1, respectively. The results show that the system is capable of capturing both static and dynamic combustion processes and exhibits a good potential for flame monitoring and combustion diagnosis. To further denote that the tomographic images are representative of the actual distributions, the reconstructed distribution of temperature and H_2O mole fraction will be compared with those obtained from computational fluid dynamics (CFD) in our future work.

ACKNOWLEDGMENTS

The authors gratefully acknowledge the financial support by the National Science Foundation of China (Grant Nos. 61225006 and 61327011), Fundamental Research Funds for the Central Universities (Grant No. 30471501), and the Program for Changjiang Scholars and Innovative Research Team in University (No. IRT1203).

[1]R. M. Spearrin, C. S. Goldenstein, J. B. Jeffries, and R. K. Hanson, "Fiber-coupled 2.7 μm laser absorption sensor for CO_2 in harsh combustion environments," Meas. Sci. Technol. **24**, 055107 (2013).
[2]M. A. Bolshov, Y. A. Kuritsyn, and Y. V. Romanovskii, "Tunable diode laser spectroscopy as a technique for combustion diagnostics," Spectrochim. Acta, Part B **106**, 45–66 (2015).
[3]O. Witzel, A. Klein, S. Wagner, C. Meffert, C. Schulz, and V. Ebert, "High-speed tunable diode laser absorption spectroscopy for sampling-free in-cylinder water vapor concentration measurements in an optical IC engine," Appl. Phys. B **109**, 521–532 (2012).
[4]R. Sur, K. Sun, J. B. Jeffries, J. G. Socha, and R. K. Hanson, "Scanned-wavelength-modulation-spectroscopy sensor for CO, CO_2, CH_4 and H_2O in a high-pressure engineering-scale transport-reactor coal gasifier," Fuel **150**, 102–111 (2015).
[5]S. T. Sanders, J. Wang, J. B. Jeffries, and R. K. Hanson, "Diode-laser absorption sensor for line-of-sight gas temperature distributions," Appl. Opt. **40**, 4404–4415 (2001).
[6]C. Liu, L. Xu, and Z. Cao, "Measurement of nonuniform temperature and concentration distributions by combining line-of-sight TDLAS with regularization methods," Appl. Opt. **52**, 4827–4842 (2013).
[7]T. York, H. McCann, and K. B. Ozanyan, "Agile sensing systems for tomography," IEEE Sens. J. **11**, 3086–3105 (2011).
[8]J. Song, Y. Hong, G. Wang, and H. Pan, "Algebraic tomographic reconstruction of two-dimensional gas temperature based on tunable diode laser absorption spectroscopy," Appl. Phys. B **112**, 529–537 (2013).
[9]A. D. Sappey, P. Masterson, E. Huelson, J. Howell, M. Estes, H. Hofvander, and A. Jobson, "Results of closed-loop coal-fired boiler operation using a TDLAS sensor and smart process control software," Combust. Sci. Technol. **183**, 1282–1295 (2011).
[10]V. Kasyutich and P. Martin, "Towards a two-dimensional concentration and temperature laser absorption tomography sensor system," Appl. Phys. B **102**, 149–162 (2011).
[11]M. P. Wood and K. B. Ozanyan, "Concentration and temperature tomography at elevated pressures," IEEE Sens. J. **13**, 3060–3066 (2013).
[12]F. Wang, K. F. Cen, N. Li, J. B. Jeffries, Q. X. Huang, J. H. Yan, and Y. Chi, "Two-dimensional tomography for gas concentration and temperature distributions based on tunable diode laser absorption spectroscopy," Meas. Sci. Technol. **21**, 045301 (2010).
[13]L. Wondraczek, A. Khorsandi, U. Willer, G. Heide, W. Schade, and G. H. Frischat, "Mid-infrared laser-tomographic imaging of carbon monoxide in laminar flames by difference frequency generation," Combust. Flame **138**, 30–39 (2004).
[14]L. Ma, X. Li, S. T. Sanders, A. W. Caswell, S. Roy, D. H. Plemmons, and J. R. Gord, "50-kHz-rate 2D imaging of temperature and H_2O concentration at the exhaust plane of a J85 engine using hyperspectral tomography," Opt. Express **21**, 1152–1162 (2013).
[15]W. Cai and C. F. Kaminski, "A tomographic technique for the simultaneous imaging of temperature, chemical species, and pressure in reactive flows using absorption spectroscopy with frequency-agile lasers," Appl. Phys. Lett. **104**, 034101 (2014).
[16]Y. Deguchi, T. Kamimoto, Z. Z. Wang, J. J. Yan, J. P. Liu, H. Watanabe, and R. Kurose, "Applications of laser diagnostics to thermal power plants and engines," Appl. Therm. Eng. **73**, 1453–1464 (2014).
[17]Y. Huang and V. Yang, "Dynamics and stability of lean-premixed swirl-stabilized combustion," Prog. Energy Combust. Sci. **35**, 293–364 (2009).
[18]C. Liu, L. Xu, J. Chen, Z. Cao, Y. Lin, and W. Cai, "Development of a fan-beam TDLAS-based tomographic sensor for rapid imaging of temperature and gas concentration," Opt. Express **23**, 22494–22511 (2015).
[19]L. Xu, C. Liu, D. Zheng, Z. Cao, and W. Cai, "Digital signal processor-based high-precision on-line Voigt lineshape fitting for direct absorption spectroscopy," Rev. Sci. Instrum. **85**, 123108 (2014).
[20]L. Xu, T. Wei, J. Zhou, and Z. Cao, "Modified Landweber algorithm for robust particle sizing by using Fraunhofer diffraction," Appl. Opt. **53**, 6185–6193 (2014).
[21]W. Q. Yang, D. M. Spink, T. A. York, and H. McCann, "An image-reconstruction algorithm based on Landweber's iteration method for electrical-capacitance tomography," Meas. Sci. Technol. **10**, 1065–1069 (1999).
[22]P. C. Hansen and M. Saxild-Hansen, "AIR tools—A MATLAB package of algebraic iterative reconstruction methods," J. Comput. Appl. Math. **236**, 2167–2178 (2012).
[23]F. Li, X. Yu, H. Gu, Z. Li, Y. Zhao, L. Ma, L. Chen, and X. Chang, "Simultaneous measurements of multiple flow parameters for scramjet characterization using tunable diode-laser sensors," Appl. Opt. **50**, 6697–6707 (2011).
[24]C. Liu, L. Xu, Z. Cao, and H. McCann, "Reconstruction of axisymmetric temperature and gas concentration distributions by combining fan-beam TDLAS with onion-peeling deconvolution," IEEE Trans. Instrum. Meas. **63**, 3067–3075 (2014).
[25]C. Zheng, W. Ye, J. Huang, T. Cao, M. Lv, J. Dang, and Y. Wang, "Performance improvement of a near-infrared CH_4 detection device using wavelet-denoising-assisted wavelength modulation technique," Sens. Actuators, B **190**, 249–258 (2014).
[26]P. Wright, K. B. Ozanyan, S. J. Carey, and H. McCann, "Design of high-performance photodiode receivers for optical tomography," IEEE Sens. J. **5**, 281–288 (2005).
[27]J. G. Graeme, *Photodiode Amplifiers: Op AMP Solutions* (McGraw-Hill, New York, 1995).